

# Pupil remapping for high contrast astronomy: results from an optical testbed

T. Kotani<sup>1</sup>, S. Lacour<sup>1,2\*</sup>, G. Perrin<sup>1</sup>, G. Robertson<sup>2</sup> and P. Tuthill<sup>2</sup>

<sup>1</sup>*LESIA, Observatoire de Paris, CNRS/UMR 8109, 92190 Meudon, France*

<sup>2</sup>*School of Physics, Sydney University, NSW 2006, Australia*

*\*Corresponding author: [sylvestre.lacour@obspm.fr](mailto:sylvestre.lacour@obspm.fr)*

**Abstract:** The direct imaging and characterization of Earth-like planets is among the most sought-after prizes in contemporary astrophysics, however current optical instrumentation delivers insufficient dynamic range to overcome the vast contrast differential between the planet and its host star. New opportunities are offered by coherent single mode fibers, whose technological development has been motivated by the needs of the telecom industry in the near infrared. This paper presents a new vision for an instrument using coherent waveguides to remap the pupil geometry of the telescope. It would (i) inject the full pupil of the telescope into an array of single mode fibers, (ii) rearrange the pupil so fringes can be accurately measured, and (iii) permit image reconstruction so that atmospheric blurring can be totally removed. Here we present a laboratory experiment whose goal was to validate the theoretical concepts underpinning our proposed method. We successfully confirmed that we can retrieve the image of a simulated astrophysical object (in this case a binary star) through a pupil remapping instrument using single mode fibers.

© 2021 Optical Society of America

**OCIS codes:** (350.1260) Astronomical optics; (060.2430) Fibers, single-mode; (070.6110) Spatial filtering; (120.3180) Interferometry.

---

## References and links

1. M. Mayor and D. Queloz, "A Jupiter-Mass Companion to a Solar-Type Star," *Nature (London)* **378**, 355–+ (1995).
2. S. Seager, B. A. Whitney, and D. D. Sasselov, "Photometric Light Curves and Polarization of Close-in Extrasolar Giant Planets," *Astrophys. J.* **540**, 504–520 (2000). [arXiv:astro-ph/0004001](https://arxiv.org/abs/astro-ph/0004001).
3. G. Chauvin, A.-M. Lagrange, C. Dumas, B. Zuckerman, D. Mouillet, I. Song, J.-L. Beuzit, and P. Lowrance, "A giant planet candidate near a young brown dwarf. Direct VLT/NACO observations using IR wavefront sensing," *A&A* **425**, L29–L32 (2004). [arXiv:astro-ph/0409323](https://arxiv.org/abs/astro-ph/0409323).
4. C. Marois, B. Macintosh, T. Barman, B. Zuckerman, I. Song, J. Patience, D. Lafreniere, and R. Doyon, "Direct Imaging of Multiple Planets Orbiting the Star HR 8799," *Science* **322**, 1348–1352 (2008). [arXiv:astro-ph/0811.2606](https://arxiv.org/abs/astro-ph/0811.2606).
5. O. Guyon, "Limits of Adaptive Optics for High-Contrast Imaging," *Astrophys. J.* **629**, 592–614 (2005). [arXiv:astro-ph/0505086](https://arxiv.org/abs/astro-ph/0505086).
6. A. . Lagrange, D. Gratadour, G. Chauvin, T. Fusco, D. Ehrenreich, D. Mouillet, G. Rousset, D. Rouan, F. Allard, E. Gendron, J. Charton, L. Mugnier, P. Rabou, J. Montri, and F. Lacombe, "A probable giant planet imaged in the Beta Pictoris disk," *ArXiv e-prints* **491**, 883–888 (2008). [arXiv:astro-ph/0811.3583](https://arxiv.org/abs/astro-ph/0811.3583).
7. A. Labeyrie, "Attainment of Diffraction Limited Resolution in Large Telescopes by Fourier Analysing Speckle Patterns in Star Images," *A&A* **6**, 85–+ (1970).

8. C. A. Haniff, C. D. Mackay, D. J. Titterton, D. Sivia, and J. E. Baldwin, "The first images from optical aperture synthesis," *Nature (London)* **328**, 694–696 (1987).
9. P. G. Tuthill, J. D. Monnier, W. C. Danchi, E. H. Wishnow, and C. A. Haniff, "Michelson Interferometry with the Keck I Telescope," *Astron. Soc. Pac.* **112**, 555–565 (2000). [arXiv:astro-ph/0003146](#).
10. S. Lacour, S. Meimon, E. Thiébaud, G. Perrin, T. Verhoelst, E. Pedretti, P. A. Schuller, L. Mugnier, J. Monnier, J. P. Berger, X. Haubois, A. Poncelet, G. Le Besnerais, K. Eriksson, R. Millan-Gabet, S. Ragland, M. Lacasse, and W. Traub, "The limb-darkened Arcturus: imaging with the IOTA/IONIC interferometer," *A&A* **485**, 561–570 (2008). [arXiv:astro-ph/0804.0192](#).
11. G. Perrin, S. Lacour, J. Woillez, and É. Thiébaud, "High dynamic range imaging by pupil single-mode filtering and remapping," *Mon. Not. R. Astron. Soc.* **373**, 747–751 (2006). [arXiv:astro-ph/0609362](#).
12. S. Lacour, E. Thiébaud, and G. Perrin, "High dynamic range imaging with a single-mode pupil remapping system: a self-calibration algorithm for redundant interferometric arrays," *Mon. Not. R. Astron. Soc.* **374**, 832–846 (2007). [arXiv:astro-ph/0610458](#).
13. V. Coude Du Foresto, S. Ridgway, and J.-M. Mariotti, "Deriving object visibilities from interferograms obtained with a fiber stellar interferometer," *A&AS* **121**, 379–392 (1997).
14. J. D. Monnier, E. Pedretti, N. Thureau, J.-P. Berger, R. Millan-Gabet, T. ten Brummelaar, H. McAlister, J. Sturmman, L. Sturmman, P. Muirhead, A. Tannirkulam, S. Webster, and M. Zhao, "Michigan Infrared Combiner (MIRC): commissioning results at the CHARA Array," in *Society of Photo-Optical Instrumentation Engineers (SPIE) Conference Series*, vol. 6268 of *Presented at the Society of Photo-Optical Instrumentation Engineers (SPIE) Conference* (2006).
15. H. A. McAlister, T. A. ten Brummelaar, D. R. Gies, W. Huang, W. G. Bagnuolo, Jr., M. A. Shure, J. Sturmman, L. Sturmman, N. H. Turner, S. F. Taylor, D. H. Berger, E. K. Baines, E. Grundstrom, C. Ogden, S. T. Ridgway, and G. van Belle, "First Results from the CHARA Array. I. An Interferometric and Spectroscopic Study of the Fast Rotator  $\alpha$  Leonis (Regulus)," *Astrophys. J.* **628**, 439–452 (2005). [arXiv:astro-ph/0501261](#).
16. C. D. Mackay, R. N. Tubbs, R. Bell, D. J. Burt, P. Jerram, and I. Moody, "Subelectron read noise at MHz pixel rates," in *Society of Photo-Optical Instrumentation Engineers (SPIE) Conference Series*, M. M. Blouke, J. Canosa, and N. Sampat, eds., vol. 4306 of *Presented at the Society of Photo-Optical Instrumentation Engineers (SPIE) Conference*, pp. 289–298 (2001).
17. J. E. Baldwin, P. J. Warner, and C. D. Mackay, "The point spread function in Lucky Imaging and variations in seeing on short timescales," *A&A* **480**, 589–597 (2008).
18. E. Thiébaud, "MIRA: an effective imaging algorithm for optical interferometry," in *Society of Photo-Optical Instrumentation Engineers (SPIE) Conference Series*, vol. 7013 of *Presented at the Society of Photo-Optical Instrumentation Engineers (SPIE) Conference*, pp. 7013–53 (2008).

## 1. Introduction

Since the discovery of a giant planet around the solar-type star 51 Pegasi by Mayor & Queloz[1], over 200 extrasolar planets have been discovered, almost all by indirect methods such as radial velocity monitoring and transit observations. Selection biases inherent to these techniques helps explain the high incidence of relatively massive (Jupiter-size) planets orbiting close to their parent stars in the sample so far. At visible wavelengths, the reflected light from such an extrasolar giant planet is typically more than  $10^4$  times fainter than the direct light from its parent star[2]. Bright speckles arising naturally from the transfer function of the turbulent atmosphere are a good mimic of the expected planetary signal, compounding the difficulty of the direct imaging problem. A plethora of technologies have been advanced to tackle the high-contrast imaging problem, however it is fair to say that none so far has achieved wide success except over quite narrowly-defined niches, as discussed further below.

By partially correcting the atmospheric degradation, Adaptive Optics (AO) has led to several direct detections of extrasolar planets [3, 4]. However, the detection limit is highly dependant on the angular separation[5]. Published limits are, up to now, of the order of  $10^3$  at 500 milliarseconds, and  $10^4$  at twice that distance[6]. At smaller separations ( $1$  to  $\approx 5 \lambda/D$ ), Fourier transform deconvolution techniques is a necessary complement to AO imaging. In that domain, speckle imaging[7] and aperture masking interferometry[8, 9] that utilize post-processing of rapid-exposure data have demonstrated recovery of high contrast images. In particular, masking sets the present standard for very high angular resolution work within a few tenths of an arcsecond, although over such scales the best demonstrated dynamic range does not exceed a

few hundred. Last but not least, long-baseline optical interferometry also has a role in faint companion detection, with a dynamic range of a few  $10^3$  at angular separation of a few tens of milliarcseconds[10].

The limited dynamic ranges attained by these techniques can mostly be attributed to the fact that atmospheric turbulence is highly time-variable, resulting in difficulty with the wavefront calibration. By tackling this problem, a single-mode pupil remapping system[11] is, on the paper, an attractive solution to achieve a high dynamic range (up to  $10^6$ )[12] at the resolution limit of a telescope. The advantages of a single-mode pupil remapping system are as follows: first, the use of single-mode fibers filters out atmospheric turbulence effects, as already demonstrated by single-mode fiber long-baseline interferometry[13]. Second, the non-redundant pupil configuration eliminates redundancy noise which affects the accuracy of wavefront measurements. Third, the full pupil area of the primary mirror can be used thanks to the pupil remapping by fibers. The removal of atmospheric turbulence and redundancy noise allows almost perfect calibration of the degraded wavefront. Therefore this technique can take full advantage of the intrinsic high angular resolution of large ground-based telescopes and fully realize the aperture-related gains over and above their large photon-collecting capability.

The technique described here originally grew out from ideas for improvements to the successful aperture masking experiments which are now established at many major world observatories (e.g. Keck, Gemini, VLT). This historical legacy gives us a straightforward model to assist in constructing the arguments in favor of pupil remapping, and we draw upon this earlier work for examples. Following a brief review of the principles in Section 2, this paper presents a practical laboratory experiment which has validated the principles of the proposed instrument. We show that image reconstruction is possible, even though the pupil geometry was considerably altered. Details of the optical design for the testbed are given in Section 3. Results and conclusions are given in the final section.

## 2. Operational Principles

### 2.1. Aperture Masking

Very high dynamic range imaging requires the minimization of the number and intensity of speckles in the image. Adaptive optics has been pursued as the most conceptually straightforward (although technically demanding) solution. At visible wavelengths, a deformable mirror with a very large number of actuators is required. This is now feasible for a 4 m telescope, although there are limitations and high dynamic range very near to the central PSF is generally not obtainable. Of order 200 actuators are required to achieve basic diffraction limited imaging. However the high dynamic range performance needed for Jupiter mass planetary detection requires at least several thousands actuators in the visible, together with a high temporal sampling frequency of the wavefront. These requirements drive the adaptive optics system into technical difficulties and high cost.

An alternative is data post-processing. The family of techniques involved is mainly known as speckle imaging or speckle interferometry [7]. The fundamental idea is that blurring from atmospheric turbulence can be frozen using exposures shorter than the seeing coherence time, allowing turbulence-free spatial information to be recovered during post-processing of the data. The post-processing is performed in the spatial frequency plane, the plane conjugated to the sky plane by the Fourier transform. Speckle imaging proceeds by calibrating the energy at each spatial frequency thanks to an identical observation of an unresolved star used as a reference. If the statistical properties of the turbulence were similar for the reference star and science target then some degree of correction can be made and the image partially cleaned of seeing-related artifacts by this procedure. Unfortunately atmospheric turbulence is not stationary and rapid changes of the transfer function means that even this statistical calibration is imperfect.

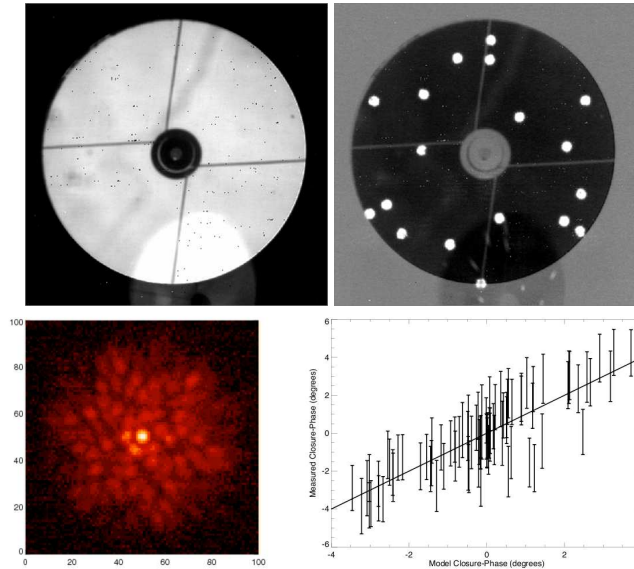


Fig. 1. A pictorial description of the aperture masking experiment now commissioned at the NAOS/CONICA camera on one of ESO's four VLT telescopes in Paranal. Top Left Panel: the unobstructed telescope pupil complete with spiders and central obstruction, as viewed in the CONICA camera. Top Right: an 18-hole aperture mask transforms the 8 m primary mirror into a sparse, non-redundant array. Note the non-ideal mask alignment visible in these engineering-test images. Lower Left: the diffraction pattern created in the image plane after using such a non-redundant pupil mask. With the adaptive optics system operating, a bright core persists at the center of the pattern, which otherwise spreads light over an area in inverse proportion to the size of the holes in the mask plate. Lower Right: this panel depicts the final data product for faint companion searches – the closure phase recovered by the data reduction software over all closed triangles of holes in the mask. For a simple unresolved point, this data product should give a value of zero (to within the limits of the random noise level). Here we see a systematic variation of the closure phase. When plotted against a model of two point-like sources, the variation betrays the presence of the high-contrast companion.

One key shortcoming of the method is that multiple different areas within the pupil telescope all contribute to the same spatial frequency in the image plane (this is called redundancy). Because different patches sum together with essentially random phases, the energy recorded at a given spatial frequency is both reduced and contaminated with seeing noise. Since decorrelation between phases increases with the distance between patches in the pupil plane, two different sets of patches (or sub-pupils) corresponding to a same spatial frequency will have less and less correlated phases leading to a suppression of the transfer function at increasing spatial frequencies: high spatial frequencies are more blurred out than low ones. These effects are all detrimental to high dynamic range imaging.

Closely related to speckle imaging is the technique of aperture masking [8]. The principles are similar to speckle imaging, but with a mask placed in a pupil plane to select only non-redundant sub-apertures. Spatial frequencies therefore correspond to unique pairs of sub-apertures from the pupil plane. As a consequence, high spatial frequencies are no longer attenuated with respect to lower spatial frequencies and the dynamic range in reconstructed images is the same at all scales. This technique has been successfully used on several telescopes. As

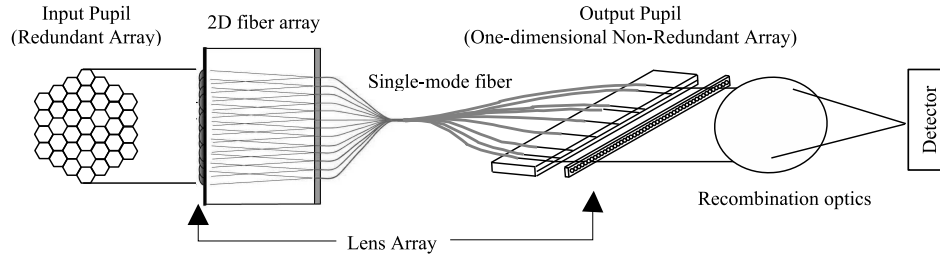


Fig. 2. A schematic diagram illustrating the principles of pupil remapping with single mode fibers. In brief, the left side depicts the pupil fragmentation and single-mode fiber injection optics, while to the right we show the spatially-filtered beams output from the fibers into a custom-designed non-redundant linear array. These elements are all described in some detail in our earlier papers[11, 12]

an example, Fig. 1 is a demonstration of faint companion detection obtained with the VLT at near-infrared wavelengths. This technique still has some drawbacks as far as dynamic range is concerned. Firstly, only a small fraction of the pupil is used: each sub-aperture has a size of the order of the Fried parameter  $r_0$ . Because of the non-redundancy requirement, only a limited number of sub-apertures are employed. The total pupil area used to collect photons (3% in the case of this VLT experiment) is illustrated by the pupil imaged in the upper panels of Fig. 1. Second, the size of sub-pupils is such that the phase varies slightly across them, inducing some decorrelation. Because the system is therefore not completely immune to phase fluctuations, some residual atmospheric turbulence noise persists in the data collected, placing limits on the dynamic range obtained.

## 2.2. Aperture masking with single-mode fibers

The problems of aperture masking can be solved by using single-mode fibers. First of all, single-mode fibers are perfect spatial filters: any light injected into a single-mode fiber will emerge as a Gaussian beam with a flat wavefront. As a consequence, wavefronts will be fully coherent after filtering with single-mode fibers. The cost of this mode cleansing is that coupling of an imperfect and variable beam into the fiber core can be low, and highly time-variable. But the final result is that the wavefront can be considered ideally flat over the entire fiber input aperture, and when separate beams filtered in this way are interfered, the data will be uncorrupted by phase corrugations. Consequently, an important source of dynamic range loss, speckle noise, is eliminated. Second, fibers are flexible optics and it is possible to use the full pupil in the input and redistribute the sub-pupils in the output in a non-redundant way. The full photon collecting capability of the telescope is therefore available for interferometric operation. The principles of the system are depicted in the sketch Fig. 2.

The instrument therefore acts to turn the telescope into a multiple-beam interferometer. Each pair of fibers maps to a specific baseline in the telescope pupil, for which a complex visibility can be measured and calibrated. An image can then be reconstructed from the full set of such visibilities by exploiting Fourier techniques already well-established across a broad range of astronomical interferometers.

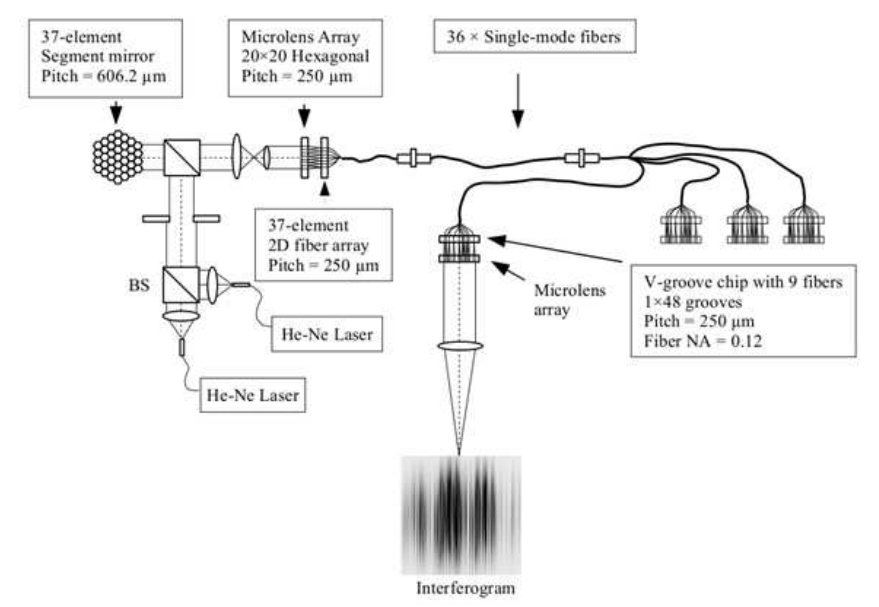


Fig. 3. Experimental setup. The optical layout of a recombining instrument is shown for only one v-groove chip. The other 3 v-groove chips may share the same recombination optics. Further details of the various components and subsystems depicted can be found in the text.

### 3. A laboratory demonstrator

#### 3.1. Overview

Two instrument concepts are under development, with the ultimate aim of providing a versatile instrument to the astronomical community. One of them called FIRST (Fibered Imager for Single Telescope) is being developed at Paris Observatory as a phase A study of the new generation of instruments to equip the CFHT (Canada-France-Hawaii Telescope) by mid-2013. The second instrument is called Dragonfly and is under development at The University of Sydney, for use at the Palomar 5m telescope as a visitor instrument.

The two instruments are similar in concept and required the setup of an optical testbed. A simple schematic for the FIRST testbed is shown in Fig. 3, which has followed a number of key design principles and components:

- Operating wavelength: 600nm to 800nm. This wavelength range is set by the cut-off wavelength of a single-mode fiber ( $\approx 550$  nm) and the sensitivity of the detector.
- Segmented Deformable Mirror is used for precise fiber coupling.
- Two-dimensional fiber array and a microlens array: the input pupil of the telescope is fragmented by a microlens array then injected into a single-mode fiber array.
- Spectrometer: the output beams from fibers are spectrally dispersed to minimize the effect of OPD and dispersion between fibers. Spectral resolution  $R \approx 100$  is required.
- Beam combiner: the output beams are recombined to measure complex visibilities of the target object.

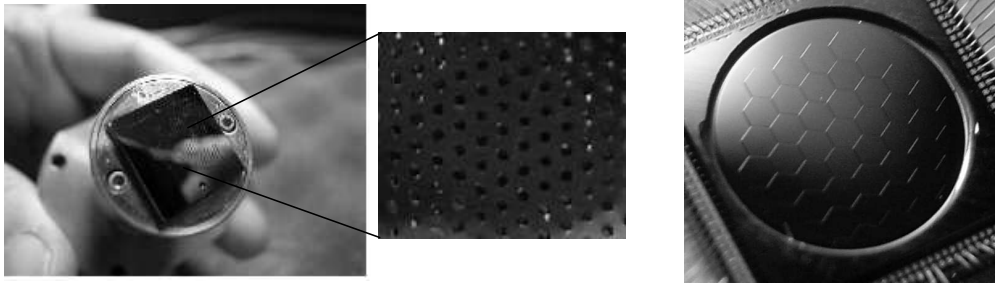


Fig. 4. Left: 2D fiber array from FiberGuide Industries. The fiber pitch is  $250\ \mu\text{m}$ . Right: Segmented deformable mirror from IRIS AO. The pitch between adjacent segments is  $606.2\ \mu\text{m}$  including a  $4\ \mu\text{m}$  gap.

To demonstrate the imaging capability of this instrument, an artificial binary star was simulated for this experiment. Two laser sources were injected into  $5\ \mu\text{m}$  pinholes to make spatially coherent point sources, and were collimated before injection into the system. One source was aligned on-axis (simulating the primary star) and the other was slightly tilted simulating an off-axis source (the companion). The two beams were then combined using a beamsplitter. A 37-element MEM, segmented deformable mirror (DM) was placed in the collimated beam to align the tip-tilt of each sub-aperture for precise injection into fibers. A second beam splitter was used to get perpendicular incidence on the DM, with a 50% return loss to the beamsplitter (the setup would not be identical on a practical instrument). After reflection by the DM, the beam diameter was reduced by a factor of 2.4, matching the pitch of adjacent sub-apertures to that of the single-mode fibers. A microlens array divided the input pupil into 36 sub-apertures, with each beam being focused onto the core of an individual fiber in the two-dimensional single-mode fiber array. This array consists of a bundle of 36 single-mode fibers precisely aligned on a hexagonal grid.

Once the light is coupled into the fibers, many of the key processing steps are then naturally achieved. These are the spatial filtering which happens in fiber, and the pupil remapping which can be trivially achieved by ensuring that the output pupil differs from the input pupil. For our testbed setup, this output fiber array took the form of a linear non-redundant array. To construct such a setup, fibers were precisely aligned in a silicon v-groove chip and the output beams from the fibers were recollimated by a linear microlens array. The beams were subsequently recombined in the image plane to make a simple Fizeau type interference pattern.

### 3.2. Injection optics

One of the most critical tasks for successful operation of this system is to realize an extremely high precision optical alignment of the bundle of 36 single-mode fibers. For optimal coupling, the position of the fiber cores must be adjusted with sub-micron precision. For this, we employed a combination of a two-dimensional fiber array, microlens array, and a segmented deformable mirror. The 2D single-mode fiber array consists of a bundle of 36 single-mode fibers fabricated by Fiber Guide Industries (Fig. 4). The fibers are packed in a hexagonal arrangement within a silicon substrate. The fiber pitch is  $250\ \mu\text{m}$ , while typical positional errors were  $\approx 1\ \mu\text{m}$  and the angular precision of fiber alignment was  $2.5\ \text{mrad}$ . The single-mode fibers used for the 2D fiber array were connectorized by Oz optics. The fiber is a polarization maintaining fiber (PM-640HP) optimized for operation in the R band with the following parameters: diameters of the fiber core/cladding are  $4$  and  $125\ \mu\text{m}$  respectively; cutoff wavelength is  $550\ \text{nm}$ ; numerical aperture is  $0.12$ . The alignment accuracy of the slow axis of the polarization state in the fibers

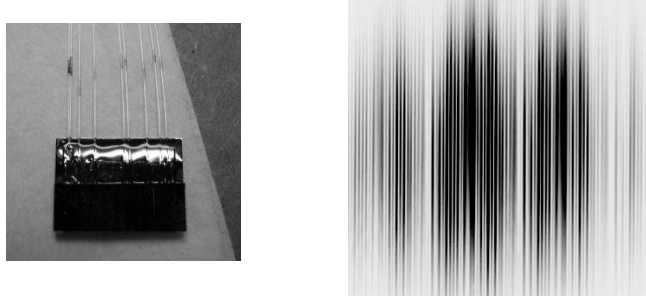


Fig. 5. Left Panel: the output linear fiber array arranged in the silicon V-groove. Right: the resultant intensity distribution displaying linear Fizeau interference fringes. Anamorphic optic is later on used to vertically collapse the fringe pattern, allowing spectral dispersion.

is  $\pm 3$  degrees. However the precision of the fiber alignment is not sufficient to achieve very high coupling efficiency and very high dynamic range. Thus we used a 37-element segmented deformable mirror based on microelectromechanical systems technology (IRIS AO) for very precise beam alignment with respect to fiber cores. Each segment consists of a hexagonal mirror attached to three individual electrostatic actuators, which provide tip-tilt and piston motion through differential actuation. An actuator has a  $5 \mu\text{m}$  stroke. The largest inscribed aperture is 3.5 mm and the center-to-center distance between two adjacent segments is  $606.2 \mu\text{m}$ , including a  $4 \mu\text{m}$  gap. This DM allows compensation of fiber position errors in the 2D fiber array. In the demonstration described here, the DM is used for static positional error compensation only, but in future it may be possible to correct the tip-tilt and piston errors arising from atmospheric turbulence using this electro-optical device.

### 3.3. Beam combiner, Anamorphic optics and Spectrometer

In order to measure fringe visibilities, output beams from the fibers need to be interferometrically recombined. We employed an image-plane combination scheme for this instrument in which fibers were arranged in a non-redundant one-dimensional array on a silicon V-groove chip from OZ optics (see Fig. 5). Such devices are widely used for telecommunication. The uniform spacing of grooves ( $250 \pm 0.5 \mu\text{m}$ ) gives precise alignment between fibers. This device is also used for the MIRC beamcombiner[14] at the CHARA interferometer[15] at Mt. Wilson. The beams from the fibers are recollimated by a linear microlens array whose lens pitch is  $250 \pm 0.5 \mu\text{m}$  (48 element linear array, SUSS MicroOptics). Then, they are recombined in the image plane to measure the object complex fringe visibilities. The non-redundant configuration is important so that any fiber pair has a unique spacing. Unfortunately, due to the limited number of detector pixels, a non-redundant, 36-element one-dimensional array is difficult to realize. To achieve sufficient fringe sampling, at least 4 pixels are needed for the highest frequency fringes to avoid aliasing problems and significant visibility loss. In the case of a 36-beam combiner, the required number of pixels is over 10000. Therefore we divided the 36 fibers into 4 sets of 9-beam combiners, with each group of 9 using one v-groove chip. For a 9-beam combiner, a 48 channel v-groove chip is used and the fibers are placed on the following positions to ensure non-redundancy: 2,3,7,14,27,29,37,43,46. The number of fringes inside the first dark ring in the PSF is about 110, which requires 440 pixels for sufficient fringe sampling. Eventually, the 4 v-groove chips may share the same set of recombination optics.

For white light operation using an incoherent source, the optical pathlength through each fiber pathway in the interferometer must be matched, as must the amount of glass pathlength. In order to relax the strict tolerance on these matching conditions, the recombined beam is spec-



trally dispersed by a prism to minimize the effect of residual Optical Path Differences (OPD) between the fibers. Because the beams are recombined one-dimensionally, the orthogonal axis can be used to disperse the light. With sufficiently high dispersion, spectral channels for the coherent fringe detection are relatively small leading to long coherence lengths. Along the dispersion direction, the diameter of the Airy pattern corresponding to one spectral resolution element must be small enough to avoid losing spectral information, while maintaining adequate sampling in the fringe direction. The system therefore requires anamorphic optics to give a differing image scale in the spatial and spectral directions. For a 9-beam combiner, the optimum diameter ratio (anamorphic ratio) is 440:1. Our design for an anamorphic system is relatively simple, using an afocal combination of two cylindrical lenses with the ratio of their focal lengths corresponding to a magnification of a pupil diameter. This results in a small PSF in the spectral dimension in the image plane. To further increase the anamorphic ratio, we added one cylindrical lens having a long focal length and having a focusing power perpendicular to the other two lenses. Zemax simulations taking into account physical optics propagation showed that the maximum anamorphic ratio of this system is 130:1. Strong spherical and chromatic aberrations from the microlens prevent the system from reaching the optimum anamorphic ratio.

Integration times for the camera must be chosen so that atmospheric piston fluctuations are frozen during an acquisition, thereby keeping the fringe contrast high. The typical atmospheric coherence time at visible wavelengths is a few milliseconds. Therefore a key requirement for the detector is very low read-out noise at very high frame rates, enabling precise fringe visibility measurements to be obtained. The EMCCD technology [16, 17] is a cost-effective solution for this purpose. Our EMCCD camera, Andor technology Luca-S, can be read at high frame-rates ( $\approx 37$  frames/sec) for reading out a full area (658x496 pixel) and effectively very small read-out noise ( $< 0.1 e^-$ ). These features allow this detector to be used in the photon noise limited regime.

#### 4. Results and Conclusions

The goal of this experiment was to demonstrate real recovery of diffraction-limited structure from an optical testbed simulating the FIRST/Dragonfly experimental methodology. Our setup for these laboratory tests is shown in Fig. 3. Although the final system should use all 36 fibers, for simplicity only 9 fibers were used for this experiment. Each input beam from a sub-aperture was precisely aligned with respect to a fiber for optimum fiber coupling by using the DM. Once the beams were aligned, the DM kept the mirror positions fixed during the measurements. We measured fringes from the artificial binary star generated by He-Ne laser illumination. The contrast ratio between the two sources was 15. Slow phase fluctuations were observed, probably thermally induced in single-mode fibers. 100 frames of image data were collected, with an integration time for each frame of 0.1 second. We fitted a binary star model to the measured visibilities. The upper panels of Fig. 6 show measured average fringe visibilities, closure phases and predictions from the best fit models. Visibility and closure phase measurement accuracies were 2% and 0.2 degrees respectively. The best-fit model is in good agreement with the measured data. A contrast ratio of  $15 \pm 1$  derived from the fitting matched well the directly measured value from a monitor CCD. The separation between the primary and the secondary source was  $0.56 \lambda/d$ , where  $d$  is a sub-aperture diameter.

In addition to the direct model fitting to the data, we reconstructed the image of the simulated binary ‘star’, using the image reconstruction software MIRA [18, Multi-Aperture Image Reconstruction Algorithm]. The lower panels of Fig. 6 show the reconstructed image (right) and the directly measured CCD image (left). Two point-like sources are clearly visible in our reconstructed image, which shows excellent agreement with the true test object yielding the same flux ratio and separation.

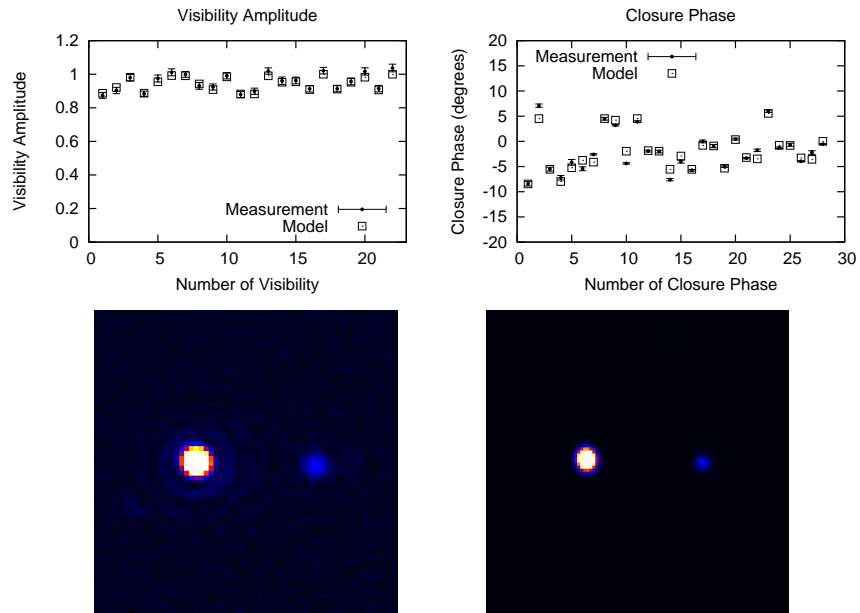


Fig. 6. Upper left panel shows measured visibility amplitudes, together with visibility predictions from the best-fit model for the simulated binary star system. Visibility measurement errors were found to be about 2%. Upper right panel shows measured closure phases and predictions from the best-fit model. The closure phase measurement error was about 0.2 degrees. Lower Left: Direct image of the simulated binary-star source. Right: Reconstructed image from complex visibility data recovered from the testbed. A byproduct of the image reconstruction algorithm is to deconvolve the point spread function, effectively removing on the reconstructed image the Airy rings caused by diffraction.

Our experiments have demonstrated the good data quality and the image reconstruction capability of a pupil remapping system using single-mode fibers for a single telescope. Thanks to the segmented deformable mirror, each input beam from a sub-aperture can be aligned very precisely with respect to a fiber, allowing excellent fiber coupling. The fringe visibilities obtained from the artificial binary star in the laboratory were in good accord with expectations from the theoretical model. Closure phases have been measured with 0.2 degree stability and fringe visibilities with 2% accuracy. Moreover, we successfully reconstructed the original image from the visibilities using the MIRA image reconstruction algorithm. This experiment is therefore an important step toward realizing an on-sky operational system.